



Full Text View

[Volume 29, Issue 9 \(September 1999\)](#)

Journal of Physical Oceanography

Article: pp. 2350–2369 | [Abstract](#) | [PDF \(907K\)](#)

Dynamical Analysis of Seasonal and Interannual Variability in the Equatorial Pacific*

Xuri Yu

School of Oceanography, University of Washington, Seattle, Washington

Michael J. McPhaden

Pacific Marine Environmental Laboratory, National Oceanic and Atmospheric Administration, Seattle, Washington

(Manuscript received May 13, 1998, in final form October 26, 1998)

DOI: 10.1175/1520-0485(1999)029<2350:DAOSAI>2.0.CO;2

ABSTRACT

Time series measurements from the Tropical Atmosphere Ocean array during the 1980s and 1990s are used to analyze the dynamics of the long-term mean, the seasonal cycle, and interannual variability in the upper 250 m of the equatorial Pacific. The analysis is based on a diagnosis of the zonal momentum equation using surface winds, ocean temperatures, and currents between 165° E and 110°W along the equator. In the mean, the balance is mainly between zonal wind stress and depth-integrated zonal pressure gradient, in good agreement with linear Sverdrup theory. For the seasonal cycle, the balance is mainly between wind stress, pressure gradient, and local acceleration, with differences between the stress and pressure gradient leading to accelerations and decelerations of the South Equatorial Current and Equatorial Undercurrent. On interannual timescales, local acceleration is much smaller than either zonal wind stress or zonal pressure gradient, indicating that to zeroth order, variations in the equatorial Pacific are in quasi-equilibrium with the wind forcing. Consistent with this quasi-equilibrium balance, Equatorial Undercurrent transports in the thermocline vary nearly in phase with the strength of the zonal pressure gradient and the easterly trade winds. Nonlinear effects are significant on all timescales, though of secondary importance in the depth-integrated zonal momentum balance.

1. Introduction

Ocean–atmosphere interactions in the tropical Pacific Ocean have been a source

Table of Contents:

- [Introduction](#)
- [Data and processing](#)
- [Description of spatial](#)
- [Zonal momentum analysis](#)
- [Discussion and conclusions](#)
- [REFERENCES](#)
- [TABLES](#)
- [FIGURES](#)

Options:

- [Create Reference](#)
- [Email this Article](#)
- [Add to MyArchive](#)
- [Search AMS Glossary](#)

Search CrossRef for:

- [Articles Citing This Article](#)

Search Google Scholar for:

- [Xuri Yu](#)
- [Michael J. McPhaden](#)

of great interest in recent years because of their influence on the El Niño–Southern Oscillation (ENSO) phenomenon, a perturbation of the climate systems that affects the lives of millions of people around the globe. From an oceanographic perspective, understanding the processes that give rise to sea surface temperature (SST) anomalies on ENSO timescales is of crucial importance. These anomalies in many respects represent a year-to-year modulation in the mean seasonal cycle (e.g., [Gu and Philander 1995](#)) and are strongly determined by dynamical processes operating in the upper ocean (e.g., [Seager et al. 1988](#); [Hayes et al. 1991](#); [Chang 1993, 1994](#); [Chen et al. 1994](#); [Kessler and McPhaden 1995](#)). Hence, a better description and understanding of the dynamics of seasonal-to-interannual variability is required in the tropical Pacific for climate model development and validation. In particular, proper representation of these dynamical processes in ocean models and coupled ocean–atmosphere models is necessary for accurate simulation and forecasting of seasonal-to-interannual climate variability (e.g., [Cane et al. 1986](#); [Battisti 1988](#); [Battisti and Hirst 1989](#); [Suarez and Schopf 1988](#); [Neelin 1991](#); [Neelin et al. 1992](#); [Mechoso et al. 1995](#)).

Aside from the imperatives of climate prediction, oceanographers have long been interested in the dynamics governing the circulation of the tropical oceans. The first modern theory of wind-driven ocean circulation was formulated to explain the existence of the North Equatorial Countercurrent in the tropical Pacific ([Sverdrup 1947](#)). The discovery of the Equatorial Undercurrent (EUC) in the early 1950s (Montgomery and Stroup 1961) spawned a host of theoretical interpretations of this subsurface eastward flow (reviewed in [McPhaden 1986](#)). Among early studies, [Arthur \(1959\)](#) showed how Sverdrup theory was consistent with the dynamics of the EUC, and could have been used to predict its existence before it was discovered.

Sverdrup theory describes the steady-state wind-driven circulation of the ocean. However, winds vary significantly across a broad range of frequencies, and the ocean adjusts to these wind changes through the excitation and propagation of planetary waves. The time it takes for these waves to cross the basin and to set up zonal pressure gradients in balance with the wind stress, compared to the timescale on which the winds vary, determines whether the ocean will be in equilibrium. At midlatitudes, planetary waves propagate too slowly to adjust the ocean to equilibrium on seasonal-to-interannual timescales. Near the equator, planetary waves (namely equatorial Rossby and Kelvin waves) propagate much more rapidly such that in principle it is possible for the ocean to approach Sverdrup equilibrium to wind forcing on relatively short timescales ([Philander 1979](#)).

The Sverdrup momentum balance on the equator reduces to the simple expression

$$P_x = \tau_0^x,$$

where P_x is the depth-integrated zonal pressure gradient and τ_0^x is the surface zonal wind stress. In the equatorial Atlantic, a basin three times narrower than the Pacific, both models and observations indicate that equatorial waves set up pressure gradients sufficiently quickly to balance seasonal and lower frequency wind stress changes ([Katz 1977, 1987](#); [Cane and Sarachik 1981](#); [Philander and Pacanowski 1981](#); [Katz et al. 1995](#)). In the equatorial Pacific, the situation is less clear. In principle, the seasonal cycle should not be in equilibrium with wind forcing along the equator because the basin is too wide for waves to cross it and to set up zonal pressure gradients on timescales short compared to a season. Moreover, annual period Rossby and Kelvin waves have been observed in the tropical Pacific (e.g., [Lukas and Firing 1985](#); [Kessler and McCreary 1993](#); [Yu and McPhaden 1999](#)) and are presumably important in generating circulation features such as the springtime reversal of the South Equatorial Current (SEC) ([Yu et al. 1997](#); [Yu and McPhaden 1999](#)). On interannual timescales, equatorial waves form the cornerstone of many theories of ENSO, such as the delayed oscillator ([Battisti 1988](#); [Suarez and Schopf 1988](#)), and these waves are evident in many empirical analyses of ENSO variability (e.g., [Picaut and Delcroix 1995](#); [Boulangier and Menkes 1995](#)).

Up to the present, empirical diagnosis of the Sverdrup momentum balance on seasonal-to-interannual timescales in the equatorial Pacific has been limited by inadequate data. It is unclear exactly how far from steady equilibrium the equatorial Pacific Ocean is near the equator, given the conflicting results of previous observational tests of the Sverdrup momentum balance (e.g., [Meyers 1979](#); [Tsuchiya 1979](#); [Mangum and Hayes 1984](#); [McPhaden and Taft 1988](#)). The purpose of this study is therefore to assess the degree to which the equatorial Pacific Ocean behaves according to the Sverdrup momentum balance on seasonal-to-interannual timescales, and the implications of this balance (or lack thereof) for current variations along the equator. To achieve this objective, we follow the methodology used in [McPhaden and Taft \(1988\)](#), who used 2½ years of moored time series measurements of surface winds, temperatures, and currents in the eastern equatorial Pacific (110–140°W) collected as part of the Equatorial Pacific Ocean Climate Studies (EPOCS) Program ([Hayes et al. 1986](#)) and TROPIC HEAT Program ([Eriksen 1985](#)). [McPhaden and Taft \(1988\)](#) concluded that $P_x = \tau_0^x$ applied on seasonal timescales, to within the errors of their analysis. However, these errors were relatively large, given the shortness of the records used compared to the timescale of the seasonal cycle. Their data records were also too short to analyze the dynamics of interannual variability. But for the 2½-year record length mean, they found that the eastern Pacific equatorial Pacific was close to Sverdrup equilibrium.

We will expand on the analysis of [McPhaden and Taft \(1988\)](#) to incorporate many more years of moored time series data

and to incorporate a much wider range of longitudes (110°W–165°E) in the analysis. We will rely primarily on data from the Tropical Atmosphere Ocean (TAO) Array, which consists of about 70 moorings spanning the equatorial Pacific basin between about 8°S and 8°N ([McPhaden et al. 1998](#)). The array measures surface winds, ocean temperatures, and ocean currents. Many of the sites have been instrumented for a sufficiently long period (more than 6 years) to compute reliable monthly mean climatologies and to estimate interannual variability.

There are several advantages of using TAO data for this study. One is that high-frequency variability, which might otherwise be aliased in infrequent shipboard measurements, can be averaged out, yielding more sharply defined low-frequency variability. Another is that contemporaneous data for winds, SST, and upper-ocean temperatures are available with similar temporal/spatial resolution and cover large regions not routinely sampled by standard shipping routes. Finally, unique to the TAO data is the ability to measure upper-ocean velocity at several mooring sites along the equator (q.v. [McPhaden and McCarty 1992](#); [McCarty and McPhaden 1993](#)).

The remainder of this paper is organized as follows. [Section 2](#) provides a detailed description of the datasets and processing procedures used in this study. [Section 3](#) then illustrates various aspects of seasonal-to-interannual variability in the equatorial Pacific using TAO data. [Section 4](#) describes the diagnosis of the zonal momentum equation, followed by discussion and conclusions in [section 5](#).

2. Data and processing

a. The TAO buoy array

The TAO Array was implemented as part of the Tropical Ocean Global Atmosphere program to monitor, understand, and predict seasonal-to-interannual climate variability. The array presently consists of nearly 70 deep ocean moorings with 2°–3° meridional spacing and 10°–15° longitudinal spacing across the equatorial Pacific, spanning 8°S to 8°N ([Fig. 1a](#)). Most of these buoys are Autonomous Temperature Line Acquisition System (ATLAS) thermistor chain moorings ([Hayes et al. 1991](#)), which measure SST (nominally at 1-m depth) and temperatures at 10 subsurface depths down to 500 m. ATLAS moorings also measure surface winds, relative humidity, and air temperatures. Mechanical current meters (MCM) and acoustic Doppler current profilers (ADCP) provide velocity measurements at five locations along the equator ([Fig. 1a](#)), collecting time series of currents in the upper 250–300 m ([McPhaden 1993](#)). The MCMs started operation at 140°W and 110°W in the early 1980s and at 165°E in the mid-1980s. ADCPs were installed at all five locations indicated in [Fig. 1a](#) in the early 1990s except at 170°W, where ADCPs were first deployed in 1988 ([Weisberg and Hayes 1995](#)). Data are sampled at 15-min to 2-h intervals depending on the instrument, then processed to daily averages. Details of sampling characteristic instrumentation and measurement errors can be found in [McPhaden and McCarty \(1992\)](#), [McCarty and McPhaden \(1993\)](#), [Mangum et al. \(1994\)](#), and [Plimpton et al. \(1997a,b\)](#).

In this study, we will use only time series of surface winds, sea temperatures, and currents along the equator with length of 6 years or longer by May of 1997. Timelines for each mooring site are shown in [Fig. 1b](#). Overall data return for winds, temperatures, and currents is about 85%.

To reduce missing data for surface winds and ocean temperatures at the equator, averages between 2°S and 2°N are used to fill gaps based on high meridional coherence within 2° of the equator ([Harrison and Luther 1990](#); [Kessler et al. 1996](#)). A different method is used to fill gaps in zonal velocity time series since there are no nearby moored velocity measurements off the equator. We start with MCM time series at 165°E, 140°W, and 110°W since they are longer than those from the ADCPs. Measurements of currents from the two different types of current meters are highly correlated ([Plimpton et al. 1997b](#)), so records from the ADCPs are used to fill gaps in the time series from the MCMs at these three longitudes when available. At 170°W, the ADCP time series only are used because there are no MCM data at this location.

After filling data gaps using these methods, remaining gaps 3 months wide or less are filled by linear interpolation in time. This method works reasonably well for seasonal and ENSO timescales, which are the primary focus of our study. Data at 125°W before 1988 and the velocity data at 170°W after 1994 are not used in this study because of the large gaps in these time series.

Most ADCPs at 170°W were upward looking and mounted on a subsurface float, so measurements of velocity above 30 m were contaminated by sidelobe reflections ([Plimpton et al. 1997b](#)). In order to generate a time series of velocity at 10-m depth, which is shallowest depth of velocity measurements at other locations, we derived a 10-m record from linear extrapolation of records at depths 30 and 40 m. We tested the accuracy of the procedure using data at 0°, 140°W where an extrapolated time series could be compared with an actual 10-m time series. Actual and extrapolated time series of monthly mean zonal velocity had a cross-correlation coefficient of 0.96, and the standard deviation of the differences was about 6 cm s⁻¹. However, the record length mean of the extrapolated time series was too strong to the west by 11 cm s⁻¹. Whereas vertical shears on which this extrapolation is based are stronger at 140°W than 170°W, the test nonetheless points out a potential for our shallow 10–20-m velocity estimates at 0°, 170°W to be biased westward by several centimeters per second.

Time series of daily averaged winds are used to compute surface wind stress, which is defined as

$$\tau = \rho_a C_d |\mathbf{U}| \mathbf{U},$$

where τ is vector surface wind stress, ρ_a is the air density, C_d is the drag coefficient, and \mathbf{U} is the vector wind speed. The winds at 10 m above the sea surface are estimated from TAO observations at 4 m using the algorithm described in [daSilva et al. \(1994\)](#), assuming a neutrally stable surface boundary layer. The air density and drag coefficient are set at 1.225 kg m^{-3} and 1.2×10^{-3} . Uncertainty in C_d may lead to errors of $\pm 10\%$ in wind stress ([Zeng et al. 1998](#)).

Dynamic height is calculated relative to 500 dbar from daily averaged temperatures from the TAO and a mean temperature–salinity relationship based on the [Levitus and Boyer \(1994\)](#) and [Levitus et al. \(1994\)](#) temperature and salinity climatologies. The root-mean-square error for the calculation is about 3–4 dyn cm in the western Pacific and 2–3 dyn cm in the eastern Pacific, mainly due to the use of the mean temperature–salinity relationship, neglected variability below 500 dbar, and relatively coarse vertical resolution of the TAO temperature observations ([Busalacchi et al. 1994](#)).

b. Estimates of means, seasonal, and interannual variations

Mean climatologies of surface stress, temperatures, surface dynamic height, and currents are calculated from time series over a period of January 1988–December 1996. The climatologies are smoothed by a 2-month running-mean filter twice (i.e., 3-month triangle filter) to remove the intraseasonal variability ([Kessler and McPhaden 1995](#); [Kessler et al. 1995](#)). Ninety percent confidence intervals for monthly climatologies are based on year-to-year variations around the mean climatology, using the Student’s t-distribution, assuming that each year is independent. Seasonal variations around the means are obtained by subtracting the annual means from the mean climatologies. In a previous paper, we demonstrated that the climatologies compiled from the TAO data are well defined and are consistent with climatologies from other datasets ([Yu and McPhaden 1999](#)). Interannual variations around the mean seasonal cycle are smoothed by a 13-month running-mean filter and 3-month triangle filter to remove frequencies equal or higher than 12 months after mean climatologies are subtracted from the time series.

3. Description of spatial and temporal variations

a. Examples of time series

[Figure 2](#) shows, as an example, time series of surface stress, temperatures, and zonal currents at $0^\circ, 110^\circ\text{W}$ where the records are the longest. At this location, both zonal and meridional stress have strong seasonal variations, but interannual variations are relatively weak. Sea surface temperature displays large variations on both seasonal and interannual timescales, while thermocline temperatures have more pronounced interannual signals. Evident in the time series are warm SSTs and a deep thermocline in El Niño years (i.e., 1982–83, 1986–87, 1991–92, and 1994–95). Weak La Niña events occurred in 1984–85 and 1995–1996, and a strong La Niña event occurred in 1988–89.

Zonal currents show strong variations in both surface and subsurface layers at this location ([Fig. 2c](#)). One of the most prominent features is the reversal of the normally westward flowing South Equatorial Current (SEC) in late boreal spring and early summer of almost every year. Flow at these times is against the easterly trade winds in the eastern Pacific. The dynamics of this “springtime reversal” ([Halpern 1987](#)) have been a subject of several recent studies ([Philander et al. 1987](#); [McPhaden and Taft 1988](#); [Philander and Chao 1991](#); [Yu et al. 1997](#); [Yu and McPhaden 1999](#)).

b. Seasonal and interannual variations

[Figure 3](#) displays time series of seasonal variations around the annual means in winds, temperatures, and zonal currents at $165^\circ\text{E}, 170^\circ\text{W}, 140^\circ\text{W},$ and 110°W at the equator. Zonal and meridional winds have largest seasonal variations in the eastern Pacific. Temperatures exhibit significant seasonal variations at all four longitudes with maxima in the thermocline except at 110°W , where the maximum variation is found near the surface. Zonal currents have significant seasonal variations at all four longitudes. At each longitude, the currents are approximately in phase vertically above the EUC core with maximum variations usually above the core, but below the surface. Note that the surface winds at 170°W vary only weakly on seasonal timescales, but the seasonal variations in zonal currents at this location are as large as at 140°W and 110°W .

Interannual fluctuations, illustrated at $0^\circ, 110^\circ\text{W}$ and $0^\circ, 165^\circ\text{E}$ ([Fig. 4](#)), are dominated by ENSO timescale variations. Zonal wind stress variations on interannual timescales are larger in the western Pacific than in the far eastern Pacific. Conversely, meridional wind stress variations are stronger in the eastern Pacific than in the western Pacific because of meridional shifts in the position of the intertropical convergence zone (ITCZ). Interannual variations in zonal currents are

comparable to seasonal variations (Figs. 3 and 4), but unlike seasonal variations, interannual variations in zonal currents do not have strong vertical coherence and are not trapped above the EUC core. Interannual variations in temperature have high coherence in and above the thermocline at 110°W with maximum amplitudes in the thermocline between 50 and 100 m. At 165°E, maximum temperature amplitudes are also found in the thermocline at depths of 100–200 m, but these are less coherent with surface temperature variations compared to farther east. The SST anomaly is large at 110°W because the mean thermocline is very shallow there and SST variations are dominated by anomalous vertical displacements of the thermocline (Battisti and Sarachik 1995).

Interannual variations along the equator for winds, SST, thermocline depth, dynamic height, and zonal transport per unit width in the EUC (depths between 80 and 200 m) are shown in Fig. 5. Only data from 1988 to 1996 are presented due to the limited extent of the TAO array before 1988 (Fig. 1b). The 18°C instead of 20°C isotherm is shown because the 20°C isotherm breaks the surface during the 1988–89 La Niña. Zonal transport per unit width is shown only through September 1993 (Fig. 5e) because velocity data at 170°W are available only up to March 1994 and edge effects due to smoothing the data further shorten the time series. The upper bound of 80 m for the transport calculation was chosen to avoid including flows in the surface layer that tend to be incoherent with those in the thermocline (e.g., Fig. 4). A somewhat shallower upper bound might be more appropriate for 110°W given that the undercurrent is shallower there than in the central and western Pacific. However, calculations of zonal transport per unit width over depths of 50–200 m were qualitatively very similar to those over 80–200 m, so we discuss only the latter for simplicity.

Zonal surface stress varies roughly in phase in the western and central Pacific, where it has maximum amplitudes. Variations in zonal stress in the eastern Pacific are weak and roughly 180° out of phase with those farther west. SST variations have amplitudes typically of 0.5–1.5°C. The SST anomaly is highly correlated with the depth anomaly of the 18°C isotherm in the eastern Pacific (Figs. 5b and 5c), where the mean thermocline depth is shallow.

Thermocline depth and dynamic height have very similar phase features with maximum amplitudes in the eastern Pacific (Figs. 5c and 5d). Both 18°C depth and dynamic height exhibit eastward phase propagation, but most of the phase shift occurs in the central Pacific. This phase propagation is similar to that shown in the analytic study of Cane and Sarachik (1981) and in the model simulations of Battisti and Hirst (1989) and Schneider et al. (1995). In contrast, neither SST nor surface wind stress displays similarly consistent eastward propagation from 1986 to 1996 (Figs. 5a and 5b).

Although longitude–time contours of zonal transport are constructed from only four locations along the equator, the transport variations exhibit a well-defined pattern of interannual variability (Fig. 5e). Extrema generally occur in the central Pacific between 140°W and 170°W, where variations are highly correlated with anomalous wind forcing to the west. During the La Niña event of 1988–89, when surface easterly winds were anomalously strong in the central and western Pacific, zonal transport in the central Pacific was anomalously eastward (i.e., the EUC was unusually strong). During the warm El Niño event of 1991–92, when the easterly winds relaxed in the central and western Pacific, zonal transport was anomalously westward between 140°W and 170°W (i.e., the EUC was unusually weak). Interestingly, consistent with the out of phase variation in zonal winds east and west of about 140°W, there is also a suggestion of an out of phase relationship between zonal current transports at 110°W with those at 140°W and 170°W. For example, during the La Niña of 1988–89, when the easterlies were anomalously weak in the eastern Pacific but strong farther to the west, the EUC transport was weak at 110°W but strong farther to the west. A similar east–west asymmetry in zonal wind stress and zonal current transport is evident during the 1991–92 El Niño. We will return to this issue of zonal transports in relation to wind variations in the next section.

4. Zonal momentum analysis

In this section, the dynamics of oceanic variations in the equatorial Pacific on mean, seasonal, and interannual timescales are investigated through diagnosis of the zonal momentum equation. Derivation of the diagnostic equation basically follows the methodology in McPhaden and Taft (1988).

a. Diagnostic equation

The zonal momentum equation in the stratified ocean can be written as

$$\rho(u_t + uu_x + \mathbf{v}u_y + wu_z - f\mathbf{v}) + p_x = 0 \quad (1)$$

where u , \mathbf{v} , and w are zonal, meridional, and vertical velocity components, p is pressure, ρ is density, f is the rate of earth rotation, A and K are vertical eddy viscosity and horizontal eddy viscosity, respectively; ∇ is a horizontal gradient operator.

The Coriolis term in (1) can be neglected since $f = 0$ on the equator. Estimating the vertical friction term is difficult due to vertically varying eddy viscosity and the need to compute second derivatives of zonal velocity. Second derivatives can be very noisy, particularly when estimated from data at only 7–8 depths in the upper 250 m as in most of the TAO velocity

data. To avoid this problem, we focus on the vertically integrated zonal momentum equation, although we examine the vertical structures of those terms whose vertical profiles can be reasonably well estimated. Integrating (1) from the sea surface to some depth $-H$, we have

$$\rho(\overline{u_t} + \overline{uu_x} + \overline{vu_y} + \overline{wu_z}) + \overline{p_x} = \tau_0^{(x)} - \tau_{-H}^{(x)} + \rho \nabla \cdot (\overline{K \nabla u}), (2)$$

where τ_0^x and τ_{-H}^x are zonal surface wind stress and zonal shear stress at $-H$, respectively, and the overbar over a term denotes vertical integral of the term in (1), for example,

$$\overline{q} = \int_{-H}^0 q dz,$$

where q can be any oceanic variable in (1). The term τ_{-H}^x will be estimated using

$$\tau_{-H}^x = \rho A u_z|_{-H}. (3)$$

Based on data availability, H will be set at 250 m in the western Pacific and 200 m in the central and eastern Pacific. When momentum terms are averaged zonally within a zonal region, the depth of 200 m will be used if any longitudes of this region do not have data available at 250 m. There are no velocity data at the sea surface, so the velocity data at 10 m are linearly extrapolated to the surface in order to calculate depth integrals over 200 m or 250 m consistent with the depth-integrated pressure gradient. The differences between velocity integrals to 0 m and 10 m are small (only a few percent) in any case.

The data from the TAO array are discrete in longitude, depth, and time, so finite differences are used to estimate spatial gradients and local accelerations. To relate estimates of zonal gradients to other terms in (2), we zonally average the momentum balance to get

$$\rho \left[\langle \overline{u_t} \rangle + \frac{(\overline{u_{x_e}^2} - \overline{u_{x_w}^2})}{(2\Delta x)} + \langle \overline{vu_y} \rangle + \langle \overline{wu_z} \rangle \right] + \frac{(\overline{p_{x_e}} - \overline{p_{x_w}})}{(\Delta x)} = \langle \tau_0^{(x)} \rangle - \langle \tau_{-H}^{(x)} \rangle + \rho \langle \nabla \cdot (\overline{K \nabla u}) \rangle, (4)$$

where x_e and x_w are eastern and western longitudes, respectively, and $\Delta x = x_e - x_w$. The angle brackets denote the average over these two longitudes, for example,

$$\langle q \rangle = \frac{1}{\Delta x} \int_{x_w}^{x_e} q dx.$$

Equation (4) will be used to estimate zonal momentum terms by using all available time series of TAO observations over intervals of 165°E–170°W, 170°W–140°W, and 140°W–110°W. Before computing these terms, the data are processed to 5-day averages to filter out short timescales, spatially incoherent fluctuations like inertia-gravity waves, and small-scale locally wind-forced variations. Then the mean, seasonal, and interannual variations in momentum terms are obtained through procedures described in section 2b.

Zonally-averaged gradients in (4), namely, $(\overline{u_{x_e}^2} - \overline{u_{x_w}^2})/(2\Delta x)$ and $(\overline{p_{x_e}} - \overline{p_{x_w}})/(\Delta x)$, are exact, but errors in the averages of $\rho \langle \overline{u_t} \rangle$, $\langle \tau_0^x \rangle$, and $\langle \tau_{-H}^x \rangle$ may result from having data only every 15°–30° zonally. To estimate these errors, we used the

method described in Bryden (1977) assuming that variability along the equator can be represented in terms of Fourier components in time and longitude. For seasonal-to-interannual timescales and observed zonal length scales of a few thousand kilometers (e.g., Fig. 5; see also Kessler et al. 1996; Yu and McPhaden 1999), formulas in Bryden (1977) suggest that we may underestimate the amplitude of true zonal averages across 30° of longitude by less than 8%. To test the sensitivity of our results to zonal averaging, the winds from the European Centre for Medium-Range Weather Forecasts and surface currents from drifting buoys (Reverdin et al. 1994), which have 2.5° and 5° zonal resolution, respectively, were used to calculate averages based on both end points and full zonal resolution. The comparison showed that in most cases, the errors due to the end-point averaging were small in all the three intervals concerned, as expected. However, relatively large errors in the zonal averages of zonal surface stress were found in the interval 165°E–170°W, where the seasonal

signals are weak (Fig. 3); see also Busalacchi et al. 1990; Yu and McPhaden 1999). Thus, zonal averages of mean seasonal zonal winds may affect the momentum balance between 165°E and 170°W as discussed in section 4b(2).

The shallow reference level of 500 dbar and the use of a mean temperature–salinity relationship to compute dynamic height may introduce error into our estimates of zonal pressure gradient. To assess how serious these errors may be, we compared surface pressure gradients from the TAO with those based on TOPEX/Poseidon sea level measurements for the period 1992–97, when both datasets are available. Largest differences are found in the interval 165°E–170°W (Fig. 6), where variability in the temperature–salinity relationship is strongest and the thermocline is deep. The pressure gradients from these two datasets are strongly correlated, but the amplitudes of TAO gradients are larger by about 20%. Seasonal cycles derived from these six years however do not exhibit any systematic differences (Fig. 6). We will also show in section 4b that zonal pressure gradient is vertically coherent in the upper 150 m. The favorable comparisons in Fig. 6 therefore indicate that the errors due to the shallow reference level and mean T – S relationship will not adversely affect our momentum analysis, either between 165°E and 170°W or farther east where the differences between TAO and TOPEX/Poseidon are even smaller.

Our data do not allow us to estimate the nonlinear term $\rho\langle\overline{u_y^2}\rangle$ or $\rho\langle\overline{w_z^2}\rangle$. Nor can we reliably estimate the horizontal diffusion term $\rho\langle\nabla \cdot (\overline{K\nabla u})\rangle$. Thus, in the next section we will concentrate on those terms that we can directly estimate and return to the issue of neglected nonlinearity and horizontal diffusion in section 4c.

b. Results

1) TIME MEANS

Figure 7 shows vertical profiles of mean $\langle p_x \rangle$ and $\rho\langle uu_x \rangle$ in intervals 165°E–170°W, 170°W–140°W, and 140°W–110°W. Mean local acceleration $\rho\langle u_\tau \rangle$ is not statistically different from zero and is not shown. Consistent with a weak mean surface stress in the western Pacific, the mean zonal pressure gradient is weaker in the western Pacific than in the central and eastern Pacific. In all these three intervals, $\langle p_x \rangle$ decreases with depth and is larger than zonal advection $\rho\langle uu_x \rangle$ in the upper 100 m. Below 100 m, $\rho\langle uu_x \rangle$ at some locations may be as large as $\langle p_x \rangle$ (e.g., 110°–140°W and 170°W–165°E).

Table 1 lists mean $\langle \tau_0^x \rangle$, $\langle \tau_{-H}^x \rangle$, and vertical integrals of $\langle p_x \rangle$ and $\rho\langle uu_x \rangle$ in these three zonal intervals. Results indicate that the zonal wind stress is mainly balanced by the depth-integrated zonal pressure gradient to zeroth order. Specifically, to within the errors of the analysis, $\overline{\langle p_x \rangle}$ and $\langle \tau_0^x \rangle$ are not significantly different from one another with 90% confidence. In the interval 140°–110°W, the difference between these two terms is larger, but they still agree with each other to within 20%, consistent with the previous studies of Bryden and Brady (1985), McPhaden and Taft (1988), and Wilson and Leetmaa (1988). The strongest mean zonal wind stresses and pressure gradients are between 110°W and 170°W, with both terms diminishing between 170°W and 165°E. Zonal advection is about 20% at most of either $\langle p_x \rangle$ or $\langle \tau_0^x \rangle$.

Assuming $A = 1 \text{ cm}^2 \text{ s}^{-1}$ in (3) consistent with Munk (1966) and similar to values used in equatorial ocean modeling studies (Pacanowski and Philander 1981), zonal shear stress at 250 m in the western Pacific and at 200 m in the central and eastern Pacific is one to two orders of magnitude smaller than the other terms (Table 1). Hence, although A is subject to considerable uncertainty (Peters et al. 1988), τ_{-H}^x is negligible compared to the other terms.

Therefore, we would conclude from this analysis that on a long-term average, the equatorial Pacific Ocean is basically in Sverdrup momentum balance with the zonal wind stress. The inexact balance between the mean stress and pressure gradient in Table 1 is due to relatively weak depth-integrated nonlinear terms, the horizontal diffusion term in (4), which we have not been able to directly estimate, plus any bias errors in our analysis.

2) SEASONAL FLUCTUATIONS

Figure 8 shows the depth–time contours of seasonal variations in zonal pressure gradient $\langle p_x \rangle$, local acceleration $\rho\langle u_\tau \rangle$, and zonal advection $\rho\langle uu_x \rangle$ in the intervals 165°E–170°W, 170°W–140°W, and 140°W–110°W. In these three zonal intervals, $\langle p_x \rangle$ decreases in amplitude with depth and is approximately in phase in the upper 150 m. Local acceleration, which is also vertically coherent most of the year, is comparable in amplitude to pressure gradient throughout the upper 150 m in all three zonal intervals. Like zonal velocity itself, the acceleration has a maximum below the surface but above the EUC core, which is located at depths of about 80 m in the eastern Pacific and about 180 m in the western Pacific. Significant local accelerations indicate that on seasonal timescales, ocean variations are not in equilibrium with surface forcing. Zonal

advection is generally smaller in amplitude than $\langle p_x \rangle$ and $\rho \langle u_l \rangle$ and has a less uniform vertical structure. It is comparable to either of the latter terms only around the depth of the EUC core.

Estimates of depth-integrated momentum terms in (4) are shown in Fig. 9. In the central and eastern Pacific, the vertical integral of zonal pressure gradient $\langle \bar{p}_x \rangle$ and the zonal surface stress $\langle \tau_0^x \rangle$ have similar amplitudes, but $\langle \tau_0^x \rangle$ tends to lead $\langle \bar{p}_x \rangle$ by about 2 months. In the western Pacific, seasonal fluctuations in $\langle \bar{p}_x \rangle$ are stronger than those farther to the east, whereas local surface wind stress variations are relatively weak. Vertical integrals of $\rho \langle uu_x \rangle$ are small compared with vertical integrals of $\langle p_x \rangle$ or $\rho \langle u_l \rangle$. In the interval 140°–110°W, where $\rho \langle \bar{uu}_x \rangle$ is largest, it is only about 17% of the amplitude of $\langle \bar{p}_x \rangle$ (Table 2).

Figure 9 also shows estimates of seasonal variations in zonal shear stress, $\langle \tau_{-H}^x \rangle$, at 250 m in 165°E–170°W, and 200 m in 170°–140°W and 140°–110°W (upper panels), assuming $A = 1 \text{ cm}^2 \text{ s}^{-1}$. This term generally is at least 50 times smaller than the surface stress on seasonal timescales (Table 2) and will be neglected in subsequent discussion of seasonal variability.

The relative importance of local accelerations for the mean seasonal cycle is emphasized by taking differences between zonal surface stress and zonal pressure gradient in the depth-integrated momentum equation (4),

$$\Delta F = \tau_0^x - \langle \bar{p}_x \rangle,$$

and comparing them with $\rho \langle \bar{u}_l \rangle$ (Fig. 9, lower panels). In the intervals 110°–140°W and 140°–170°W, ΔF is in phase with $\rho \langle \bar{u}_l \rangle$, and nearly of the same amplitude. These results suggest that the imbalance between zonal pressure gradient and wind stress between 110°W and 170°W goes mainly into accelerating zonal currents.

In the interval between 165°E and 170°W, however, the ΔF does not match $\rho \langle \bar{u}_l \rangle$ well in either amplitude or phase. The latter has a smaller magnitude than ΔF and leads ΔF in general by a couple of months. The error in pressure gradient due to the mean T – S relationship and the shallow reference level cannot account for the difference (Fig. 6), and allowing for zonal advection improves the balance only slightly. It is possible that neglected nonlinear terms are more significant in the western Pacific than in the eastern Pacific. On the other hand, analysis errors for the mean seasonal cycle of zonal wind stress may be larger in the western Pacific than farther east since averaging zonally may introduce relatively large errors into these estimates (see section 3).

In summary, between 110°W and 170°W, zonal surface stress and pressure gradient are the two main forces in the depth-integrated zonal momentum balance for seasonal variations. Their difference drives prominent accelerations and decelerations of seasonally varying zonal currents and transports. That these linear terms nearly balance each other between 110°W and 170°W suggests that seasonal variability of the depth-averaged equatorial circulation can be approximated by linear dynamics, with nonlinear terms being of secondary importance. The seasonal balance is less clear between 165°E and 170°W, perhaps due to errors in the analysis and/or the terms that we are not able to estimate.

3) INTERANNUAL FLUCTUATIONS

Figure 10 shows the depth–time contours of interannual variations in zonal pressure gradient $\langle p_x \rangle$, local acceleration $\rho \langle u_l \rangle$, and zonal advection $\rho \langle uu_x \rangle$ over 165°E–170°W and 140°–110°W. Figure 11 shows vertical integrals of these terms and surface wind stress $\langle \tau_0^x \rangle$. We have not shown variations in $\langle \tau_{-H}^x \rangle$ in Fig. 11 for the sake of clarity; this term is much smaller than the dominant terms in the momentum balance on interannual timescales as we found earlier for the seasonal cycle (Table 2). Also the interval over 170°–140°W is not included in Figs. 10 and 11 because the major points can be illustrated with just eastern and western Pacific time series.

The zonal pressure gradient is highly coherent in the upper 100 m in the intervals 165°E–170°W and 140°–110°W (Fig. 10). It is also in phase with $\langle \tau_0^x \rangle$, unlike for the seasonal cycle. The zonal wind stress and vertical integral of zonal pressure gradient are significantly crosscorrelated at the 90% level of confidence in these intervals (Table 3). The amplitude of the stress is about 13% smaller than that of the integrated pressure gradient between 165°E and 170°W (Fig. 11, Table 2). The difference may be due to the overestimate of zonal pressure gradient in this interval as shown in Fig. 6.

Local accelerations are smaller than the zonal pressure gradient in the upper 150 m. Moreover, vertically integrated accelerations are at least one order of magnitude smaller than either vertically integrated pressure gradient or zonal wind stress (Fig. 11, Table 2). Therefore, in contrast to variations on seasonal timescales, the ocean is in a state of quasi-equilibrium with the surface forcing on interannual timescales.

In the interval of 140°–110°W, interannual variations of zonal advection are in general significantly smaller than those in pressure gradient except around EUC core depths of about 100 m (Fig. 10). Zonal advection is also not as vertically coherent as $\langle p_x \rangle$, so upon vertical integration, its amplitude is further reduced. At most, zonal advection is only about 25% of either $\langle p_x \rangle$ or $\langle \tau_0^x \rangle$ (Table 2 and Fig. 11). West of 140°W, the amplitude of $\overline{\rho \langle uu_x \rangle}$ is even smaller compared to the pressure gradient and wind stress. These results suggest that the depth-integrated momentum balance on interannual timescales may be quasi-linear across the region of 165°E–110°W.

Dynamic theories of the EUC, both linear and nonlinear, indicate that the speed and transport of the EUC increase with increasing zonal wind stress, and vice versa (Charney and Spiegel 1971; McPhaden 1981; McCreary 1981). Linear theories further predict that maximum EUC speeds in the thermocline are found east of the maximum zonal wind stress and pressure gradient because of damped Kelvin wave radiation (McPhaden 1981; McCreary 1981). We might expect these relationships between zonal winds, pressure gradients, and EUC velocities to hold on interannual timescales given the quasi-equilibrium balance that we have found. To examine this hypothesis, we present time series of vertically integrated zonal pressure gradient and zonal transport per unit width in the thermocline (80–200 m) at the end longitudes of the three zonal averaging intervals (Fig. 12). Consistent with linear theory, cross-correlations between zonal pressure gradients and zonal transports at the east end longitudes are significantly nonzero with maxima at zero or near zero lag (Table 4). These correlations are also consistently higher than those between zonal pressure gradient and zonal transport at the west end longitudes, the latter of which are generally not significantly different from zero with 90% confidence.

We repeated this correlation analysis to examine the relationship between zonal wind stress and zonal transport variations in the thermocline on interannual timescales. As expected, results were similar to those cited above for zonal pressure gradient and zonal transports because of the near balance between $\overline{\langle p_x \rangle}$ and $\langle \tau_0^x \rangle$ along the equator. This covariability between anomalous wind stress and zonal transport at EUC depths in the thermocline is also evident in Fig. 5. Zonal transport in the central Pacific varies approximately in phase with the wind stress in the central and western Pacific. Likewise, the transport anomaly in the eastern Pacific is correlated with the wind stress forcing slightly to its west. Also consistent with linear theories, maximum variability in zonal transport anomalies occur east of the maximum variability in wind forcing, as shown in standard deviations of interannual variations in the zonal wind stress and zonal transport in Fig. 5.

c. Neglected terms

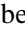
1) NONLINEARITY

We are not able to estimate nonlinear terms other than uu_x for the mean momentum balance due to lack of data. However, as shown in previous studies (Philander and Pacanowski 1980; Bryden and Brady 1985; McPhaden and Taft 1988; Qiao and Weisberg 1997), uu_x and wu_z in the mean tend to cancel each other since the EUC flows upward to the east along isopycnals. Also, uu_y tends to be small right on the equator except in the eastern Pacific. Since the nonlinear terms have smaller vertical scales than the pressure gradient term, their effects are reduced even further relative to the pressure gradient upon vertical integration. The net effect of nonlinearity is to internally redistribute zonal momentum in the upper ocean. The redistribution reduces the strength of the SEC along the equator and produces a narrower, vertically stretched EUC with larger eastward mass transports relative to that expected from linear dynamics (McPhaden 1981; McCreary 1981). Thus, the vertically integrated zonal momentum balance tends toward linearity in the mean.

We are not aware of any direct reliable estimates of nonlinear variations on seasonal-to-interannual timescales other than our own computations of uu_x . To get a sense of the expected magnitude of the nonlinear terms that cannot be directly computed, we performed a scale analysis assuming that variations on seasonal-to-interannual timescales are characterized by length scales of 2500 km zonally, 200 km meridionally, and 100 m vertically and by velocity scales of 0.5 m s^{-1} for the zonal component, 0.05 m s^{-1} for the meridional component, and 10^{-5} m s^{-1} for the vertical component. For these scales, nonlinear terms would be $O(10^{-4} \text{ N m}^{-3})$ in amplitude, and comparable in the upper 200 m to the pressure gradient term shown in Figs. 8 and 10. However, as with the uu_x , we expect that uu_y and wu_z will vary on smaller vertical scales than the pressure gradient; and that there will be a tendency for uu_x and wu_z to partially cancel one another as in the mean. Hence, upon vertical integration, we surmise that nonlinear effects on seasonal-to-interannual variations would be reduced. This inference is consistent with the generally good agreement we find between explicitly estimated terms in the linear zonal

momentum balance.

2) LATERAL DIFFUSION

We have not been able to estimate directly from our data the contribution of lateral turbulent diffusion to the mean momentum balance. Near the equator, lateral diffusivity is due mainly to nonlinear momentum fluxes associated with 20–30 day period tropical instability waves, which have their largest amplitudes between about 110°W and 140°W ([Halpern et al. 1988](#)). A major source of energy for these waves is the unstable meridional shears between the Equatorial Undercurrent and the South Equatorial Current ([Hansen and Paul 1984](#); [Luther and Johnson 1990](#)). [Bryden and Brady \(1989\)](#) estimated the magnitude of the mean lateral eddy stress to be $1.6 \times 10^{-2} \text{ N m}^{-2}$ averaged between 110°W and 152°W, based on moored time series measurements at those two longitudes. The dominant contribution to the average stress came from the meridional flux of zonal momentum at 110°W. Estimates of mean eddy stresses derived from other published reports (e.g., [Johnson and Luther 1994](#); [Qiao and Weisberg 1997](#)) are consistent with Bryden and Brady's results in both magnitude, and in the decrease in amplitude of the stresses between the eastern and central Pacific. Compared to our mean zonal pressure gradient and wind stress estimates between 110°W and 170°W ([Table 2](#) ) , lateral eddy stresses computed by [Bryden and Brady \(1989\)](#) are 2.5 to 3 times smaller. Hence, lateral diffusion may be significant in the mean zonal momentum balance of the eastern and central equatorial Pacific (particularly between 110° and 140°W), though of secondary importance relative to the mean zonal wind stress and pressure gradient.

Tropical instability waves may also contribute seasonally and interannually to the momentum balance since they are seasonally and interannually modulated ([Philander et al. 1985](#)). Unfortunately, there are no reliable estimates of the seasonal-to-interannual momentum fluxes associated with these waves. If these fluxes varied on seasonal and interannual timescales by $\pm 50\%$ of the mean value estimated by [Bryden and Brady \(1989\)](#), their amplitudes would be a significant fraction of the wind stress and zonal pressure gradient variation. [Bryden and Brady's \(1989\)](#) estimate of lateral stresses associated with instability waves may overestimate the net effect of these waves on the zonal momentum balance though. They did not consider instability wave-induced vertical momentum fluxes, which are largest in the upper thermocline above the EUC core and of opposite sign to the lateral fluxes ([Qiao and Weisberg 1997](#)). The net effect of instability waves on the zonal momentum balance would therefore need to take into account these vertical fluxes, which would tend to partially counterbalance the effects of lateral diffusion upon vertical integration.

5. Discussion and conclusions

Measurements from the TAO array have been used to analyze zonal momentum balance in the mean, and on seasonal and interannual timescales in the equatorial Pacific. In the mean, this analysis verifies that the Sverdrup momentum balance is a very good approximation for the depth-integrated circulation along the equator. This balance indicates that the mean easterly winds set up the eastward zonal pressure gradients, which in turn drives the eastward EUC in the thermocline ([Philander and Pacanowski 1980](#); [McPhaden 1981](#); [McCreary 1981](#); [Wacongne 1989](#)). Nonlinearity redistributes zonal momentum internally, but has vertical scales shorter than those of the zonal pressure gradient. Thus, in the depth-integrated momentum balance, nonlinear terms are reduced in magnitude relative to the dominant pressure gradient and wind stress terms. Lateral diffusion due to tropical instability waves is greatest in the interval 110°–140°W, but of secondary importance in the mean zonal momentum balance.

On seasonal timescales, the zonal momentum balance is mainly between surface stress, pressure gradient, and local acceleration, with the difference between surface stress and pressure gradient leading to accelerations and decelerations of the zonal currents. These accelerations indicate that wave processes are important and that on seasonal timescales the equatorial Pacific is not in equilibrium with wind forcing. Details of wave generation and propagation in the equatorial Pacific are beyond the scope of this analysis, but have been described in recent publications by [Minobe and Takeuchi \(1995\)](#) and [Yu and McPhaden \(1999\)](#).

On interannual timescales, in contrast, local acceleration is very small relative to either zonal surface wind stress or pressure gradient. The surface stress is principally balanced by the pressure gradient, suggesting that, to zeroth order, there is a quasi-equilibrium balance between wind forcing and ocean response. That the Sverdrup momentum balance holds at zeroth order does not mean, however, that equatorial waves are unimportant on interannual timescales. Although these waves are not immediately obvious from our analysis because local accelerations are small, waves are the only mechanism by which the ocean can adjust to large-scale wind forcing. The adjustment is relatively fast compared to the timescale of ENSO, which dominates interannual variability in the tropical Pacific so that explicit wave propagation is not evident.

In addition, associated with the Sverdrup momentum balance at zeroth order is an unsatisfied western boundary condition. This condition allows for time varying, nearly zonally independent fluctuations in pressure (i.e., heat content), which are the result of very low frequency wave processes pumping heat into and out of the equatorial band on ENSO timescales ([Wyrtki 1985](#); [Cane and Zebiak 1987](#); [Springer et al. 1990](#)). [Schneider et al. \(1995\)](#) showed that these wave processes are not in equilibrium with surface wind stress forcing, and that the details of anomalous thermocline topography along the equator

result from the sum of these waves plus east–west tilting in response to zonal wind stress variations. The Sverdrup momentum balance explains that part of the solution that relates wind stress variations to zonal tilts of the thermocline, but does not explain variations in zonal-mean depth of the thermocline across the basin on interannual timescales ([Cane 1992](#)).

In summary, we have used TAO data to diagnose the upper-ocean zonal momentum balance across the equatorial Pacific for the long-term mean, and for seasonal-to-interannual timescale variations. The analysis extends previous work on low-frequency equatorial ocean dynamics and adds additional insight into the role of surface wind stress forcing, zonal pressure gradient variations, and nonlinearity in affecting the circulation of the tropical Pacific. We expect that these results may contribute to progress in seasonal-to-interannual climate prediction, given that successful simulation of SST variability depends critically on proper representation of dynamical processes in the ocean component of coupled ocean–atmosphere prediction models.

Acknowledgments

The authors would like to thank Drs. William Kessler, David Battisti, Mitsuhiro Kawase, and Julian McCreary for helpful discussions and advice during the course of this work. Our thanks also extend to Jerry Davison and Dai McClurg for assisting with data processing and data presentations. The authors also wish to acknowledge use of the FERRET program for analysis and graphics in this paper. FERRET is a product of NOAA’s Pacific Marine Environmental Laboratory. This work was supported by NOAA’s Office of Global Programs and Environmental Research Laboratories. This publication is funded by the Joint Institute for the Study of the Atmosphere and Ocean (JISAO) under NOAA Cooperative Agreement NA67RJ0155.

REFERENCES

- Arthur, R. S., 1959: A review of the calculation of ocean currents at the equator. *Deep-Sea Res.*, **6**, 287–297..
- Battisti, D. S., 1988: Dynamics and thermodynamics of a warming event in a coupled atmosphere–ocean model. *J. Atmos. Sci.*, **45**, 2889–2919.. [Find this article online](#)
- , and A. C. Hirst, 1989: Interannual variability in the tropical atmosphere–ocean system: Influence of the basic state and ocean geometry. *J. Atmos. Sci.*, **46**, 1687–1711.. [Find this article online](#)
- , and E. Sarachik, 1995: Understanding and predicting ENSO. *Rev. Geophys.*, **33**, 1367–1376..
- Boullanger, J.-P., and C. Menkes, 1995: Propagation and reflection of long equatorial waves in the Pacific Ocean during the 1992–1993 El Niño. *J. Geophys. Res.*, **100**, 25 041–24 059..
- Bryden, H. L., 1977: Geostrophic comparisons of moored measurements of current and temperature during the Mid-Ocean Dynamics Experiment. *Deep-Sea Res.*, **24**, 677–681..
- , and E. C. Brady, 1985: Diagnostic model of the three-dimensional circulation in the upper equatorial Pacific Ocean. *J. Phys. Oceanogr.*, **15**, 1255–1273.. [Find this article online](#)
- , and —, 1989: Eddy momentum and heat fluxes and their effects on the circulation of the equatorial Pacific Ocean. *J. Mar. Res.*, **47**, 55–79..
- Busalacchi, A. J., M. J. McPhaden, J. Picaut, and S. R. Springer, 1990: Sensitivity of wind-driven tropical Pacific Ocean simulations on seasonal and interannual time scales. *J. Mar. Sys.*, **1**, 119–154..
- , —, and —, 1994: Variability in equatorial Pacific sea surface topography during the verification phase of the TOPEX/POSEIDON mission. *J. Geophys. Res.*, **99**, 24 725–24 738..
- Cane, M. A., 1992: Comments on “The fast-wave limit and interannual oscillations.” *J. Atmos. Sci.*, **49**, 1947–1949.. [Find this article online](#)
- , and E. S. Sarachik, 1981: The response of a linear baroclinic equatorial ocean to periodic forcing. *J. Mar. Res.*, **39**, 651–693..
- , and S. E. Zebiak, 1987: Prediction of El Niño events using a physical model. *Atmospheric and Oceanic Variability*. J. Cattel, Ed., Roy. Meteor. Soc., 153–182..
- , S. C. Dolan, and S. E. Zebiak, 1986: Experimental forecasts of the 1982/83 El Niño. *Nature*, **321**, 827–832..

Chang, P., 1993: Seasonal cycle of sea surface temperature and mixed layer heat budget in the tropical Pacific Ocean. *Geophys. Res. Lett.*, **20**, 2079–2082..

—, 1994: A study of the seasonal cycle of sea surface temperature in the tropical Pacific Ocean using reduced gravity models. *J. Geophys. Res.*, **99**, 7725–7741..

Charney, J. G., and S. L. Spiegel, 1971: The structure of wind-driven homogeneous layer near the equator. *Deep-Sea Res.*, **6**, 303–310..

Chen, D., A. J. Busalacchi, and L. M. Rothstein, 1994: The roles of vertical mixing solar radiation, and wind stress in a model simulation of the sea surface temperature seasonal cycle in the tropical Pacific Ocean. *J. Geophys. Res.*, **99**, 20 345–20 359..

daSilva, A. M., C. C. Young, and S. Levitus, 1994: *Atlas of Surface Marine Data*. Vol. 1, *Algorithms and Procedures*. NOAA Atlas NESDIS 5, 83 pp..

Eriksen, C. E., 1985: The Tropic Heat Program: An overview. *Eos, Trans. Amer. Geophys. Union*, **66**, 50–54..

Gu, D., and S. G. H. Philander, 1995: Secular changes of annual and interannual variability in the Tropics during the past century. *J. Climate*, **8**, 864–876.. [Find this article online](#)

Halpern, D., 1987: Observations of annual and El Niño thermal and flow variations along the equator 0°, 110°W and 0°, 95°W during 1980–1985. *J. Geophys. Res.*, **92**, 8197–8212..

—, R. A. Knox, and D. S. Luther, 1988: Observations of 20-day period meridional current oscillations in the upper ocean along the Pacific equator. *J. Phys. Oceanogr.*, **18**, 1514–1534.. [Find this article online](#)

Hansen, D. V., and C. A. Paul, 1984: Genesis and effects of long waves in the equatorial Pacific. *J. Geophys. Res.*, **89**, 10 431–10 440..

Harrison, D. E., and D. S. Luther, 1990: Surface winds from tropical Pacific islands: Climatological statistics. *J. Climate*, **3**, 251–271.. [Find this article online](#)

Hayes, S. P., and Coauthors, 1986: The Equatorial Pacific Ocean Climate Studies (EPOCS) plans: 1986–1988. *Eos, Trans. Amer. Geophys. Union*, **67**, 442–444..

—, L. J. Mangum, J. Picaut, A. Sumi, and K. Takeuchi, 1991: TOGA TAO: A moored array for real-time measurements in the tropical Pacific Ocean. *Bull. Amer. Meteor. Soc.*, **72**, 339–347.. [Find this article online](#)

Johnson, E. S., and D. S. Luther, 1994: Mean zonal momentum balance in the upper and central equatorial Pacific Ocean. *J. Geophys. Res.*, **99** (C4), 7689–7705..

Katz, E. J., 1977: Zonal pressure gradient along the equatorial Atlantic. *J. Mar. Res.*, **35**, 293–307..

—, 1987: Seasonal response of the sea surface to the wind in the equatorial Atlantic. *J. Geophys. Res.*, **92** (C2), 1885–1893..

—, J. A. Carton, and A. Chakraborty, 1995: Dynamics of the equatorial Atlantic from altimetry. *J. Geophys. Res.*, **100**, 25 061–25 068..

Kessler, W. S., and J. P. McCreary, 1993: The annual wind-driven Rossby wave in the subthermocline equatorial Pacific. *J. Phys. Oceanogr.*, **23**, 1192–1207.. [Find this article online](#)

—, and M. J. McPhaden, 1995: Oceanic equatorial waves and the 1991–93 El Niño. *J. Climate*, **8**, 1758–1774.. [Find this article online](#)

—, —, and K. M. Weickmann, 1995: Forcing of intraseasonal Kelvin waves in the equatorial Pacific. *J. Geophys. Res.*, **100**, 10 613–10 631..

—, M. C. Spillane, M. J. McPhaden, and D. E. Harrison, 1996: Scales of variability in the equatorial Pacific inferred from the Tropical Atmosphere–Ocean Buoy Array. *J. Climate*, **9**, 2999–3024.. [Find this article online](#)

Levitus, S., and T. P. Boyer, 1994: *World Ocean Atlas, 1994*, Volume 4, *Temperature*, NOAA Atlas NESDIS 4, Washington, DC, 117 pp..

—, —, and J. Antonov, 1994: *World Ocean Atlas, 1994*, Volume 5, *Interannual Variability of Upper Ocean Thermal Structure*, NOAA Atlas NESDIS 5, Washington, DC, 107 pp..

Lukas, R., and E. Firing, 1985: The annual Rossby wave in the central equatorial Pacific Ocean. *J. Phys. Oceanogr.*, **15**, 55–67.. [Find this article online](#)

Luther, D. S., and E. S. Johnson, 1990: Eddy energetics in the upper equatorial Pacific during the Hawaii-to-Tahiti-Shuttle Experiment. *J.*

Mangum, L. J., and S. P. Hayes, 1984: The vertical structure of the zonal pressure gradient in the eastern equatorial Pacific. *J. Geophys. Res.*, **89**, 10 441–10 449..

— , H. P. Freitag, and M. J. McPhaden, 1994: TOGA–TAO array sampling schemes and sensor evaluations. *Proc. Oceans '94 OSATES*, Vol. II, Brest, France, Mar. Technol. Soc., 402–406..

McCarty, M. E., and M. J. McPhaden, 1993: Mean seasonal cycles and interannual variations at 0°, 165°E during 1986–1992. NOAA Tech. Memo. ERL-PMEL-98, Pacific Marine Environmental Laboratory, Seattle, WA, 64 pp..

McCreary, J., 1981: A linear stratified ocean model of the equatorial undercurrent. *Philos. Trans. Roy. Soc. London*, **298**, 603–645..

McPhaden, M. J., 1981: Continuously stratified models of the steady state equatorial ocean. *J. Phys. Oceanogr.*, **11**, 337–354.. [Find this article online](#)

— , 1986: Equatorial undercurrent: 100 years of discovery. *Eos, Trans. Amer. Geophys. Union*, **67**, 762–765.

— , 1993: TOGA–TAO and the 1991–1993 El Niño–Southern Oscillation event. *Oceanography*, **6**, 36–44..

— , and B. A. Taft, 1988: Dynamics of seasonal and intraseasonal variability in the eastern equatorial Pacific. *J. Phys. Oceanogr.*, **18**, 55–67.. [Find this article online](#)

— , and M. E. McCarty, 1992: Mean seasonal cycles and interannual variations at 0°, 110°W and 0°, 140°W during 1980–1991. NOAA Tech. Memo. ERL-PMEL-95, Pacific Marine Environmental Laboratory, Seattle, WA, 118 pp..

— , and Coauthors, 1998: The Tropical Ocean Global Atmosphere (TOGA) observing system: A decade of progress. *J. Geophys. Res.*, **103**, 14 169–14 240..

Mechoso, C. R., and Coauthors, 1995: The seasonal cycle over the tropical Pacific in coupled ocean–atmosphere general circulation models. *Mon. Wea. Rev.*, **123**, 2825–2838.. [Find this article online](#)

Meyers, G., 1979: Annual variation in the slope of the 14°C isotherm along the equator in the Pacific Ocean. *J. Phys. Oceanogr.*, **9**, 885–891.. [Find this article online](#)

Minobe, S., and K. Takeuchi, 1995: Annual period equatorial waves in the Pacific Ocean. *J. Geophys. Res.*, **100** (C9), 18 379–18 392..

Montgomery, R. B., and E. D. Stroup, 1962: Equatorial waters and currents at 150°W in July–August 1952. *Johns Hopkins Oceanogr. Stud.*, No. 2, 68 pp..

Munk, W. H., 1966: Abyssal recipes. *Deep-Sea Res.*, **13**, 707–730..

Neelin, J. D., 1991: The slow sea surface temperature mode and the fast-wave limit: Analytic theory for tropical interannual oscillations and experiments in a hybrid coupled model. *J. Atmos. Sci.*, **48**, 584–606.. [Find this article online](#)

— , and Coauthors, 1992: Tropical air–sea interaction in general circulation models. *Climate Dyn.*, **7**, 73–104..

Pacanowski, R. C., and S. G. H. Philander, 1981: Parameterization of vertical mixing in numerical models of tropical oceans. *J. Phys. Oceanogr.*, **11**, 1443–1451.. [Find this article online](#)

Peters, J., M. C. Gregg, and J. M. Toole, 1988: On the parameterization of equatorial turbulence. *J. Geophys. Res.*, **93**, 1199–1218..

Philander, S. G. H., 1979: Variability of the tropical ocean. *Dyn. Atmos. Oceans*, **3**, 191–208..

— , and R. C. Pacanowski, 1980: The generation of equatorial currents. *J. Geophys. Res.*, **85**, 1123–1136..

— , and — , 1981: Response of equatorial oceans to periodic forcing. *J. Geophys. Res.*, **86**, 1903–1916..

— , and Y. Chao, 1991: On the contrast between the seasonal cycles of the equatorial Atlantic and Pacific Oceans. *J. Phys. Oceanogr.*, **21**, 1399–1406.. [Find this article online](#)

— , and Coauthors, 1985: Long waves in the equatorial Pacific Ocean. *Eos, Trans. Amer. Geophys. Union*, **66**, 154..

— , W. Hurlin, and A. Seigel, 1987: A model of the seasonal cycle in the tropical Pacific Ocean. *J. Phys. Oceanogr.*, **17**, 1986–2002.. [Find this article online](#)

Picaut, J., and T. Delcroix, 1995: Equatorial wave sequence associated with warm pool displacements during the 1986–1989 El Niño–La

Plimpton, P. E., H. P. Freitag, and M. J. McPhaden, 1997a: ADCP velocity errors from pelagic fish schooling around equatorial moorings. *J. Atmos. Oceanic Technol.*, **14**, 1212–1223..

—, —, —, and R. H. Weisberg, 1997b: Using seasonal variation of the equatorial zone geopotential gradient in the eastern Pacific Ocean moored ADCP data for fish-bias errors at 0°, 170°W. NOAA Tech. Memo. ERL-PMEL-111, Pacific Marine Environmental Laboratory, Seattle, WA, 163 pp..

Qiao, L., and R. H. Weisberg, 1997: The zonal momentum balance of the Equatorial Undercurrent in the central Pacific. *J. Phys. Oceanogr.*, **27**, 1094–1119.. [Find this article online](#)

Reverdin, G., C. Frankignoul, E. Kestenare, and M. J. McPhaden, 1994: Seasonal variability in the surface currents of the equatorial Pacific. *J. Geophys. Res.*, **99**, 20 323–20 343..

Schneider, E. K., B. Huang, and J. Shukla, 1995: Ocean wave dynamics and El Niño. *J. Climate*, **8**, 2415–2439.. [Find this article online](#)

Seager, R., S. E. Zebiak, and M. A. Cane, 1988: A model of the tropical sea surface temperature climatology. *J. Geophys. Res.*, **93**, 1265–1280..

Springer, S. R., M. J. McPhaden, and A. J. Busalacchi, 1990: Oceanic heat content variability in the tropical Pacific during the 1982–1983 El Niño. *J. Geophys. Res.*, **95**, 22 089–22 101..

Suarez, M. J., and P. S. Schopf, 1988: A delayed action oscillator for ENSO. *J. Atmos. Sci.*, **45**, 3283–3287.. [Find this article online](#)

Sverdrup, S. U., 1947: Wind-driven currents in a baroclinic ocean with application to the equatorial currents of the eastern Pacific. *Proc. Natl. Acad. Sci.*, **33**, 318–326..

Tsuchiya, M., 1979: Seasonal variation of the equatorial zone geopotential gradient in the eastern Pacific Ocean. *J. Mar. Res.*, **37**, 399–407..

Wacongne, S., 1989: Dynamical regimes of a fully nonlinear stratified model of the Atlantic Equatorial Undercurrent. *J. Geophys. Res.*, **94**, 4801–4815..

Weisberg, R. H., and S. P. Hayes, 1995: Upper ocean variability on the equator in the west-central Pacific at 170°W. *J. Geophys. Res.*, **100**, 20 485–20 498..

Wilson, D., and A. Leetmaa, 1988: Acoustic Doppler current profiling in the equatorial Pacific in 1984. *J. Geophys. Res.*, **93**, 13 947–13 966..

Wyrtki, K., 1985: Water displacements in the Pacific and the genesis of El Niño cycles. *J. Geophys. Res.*, **90**, 7129–7132..

Yu, X., and M. J. McPhaden, 1999: Seasonal variability in the equatorial Pacific. *J. Phys. Oceanogr.*, **29**, 925–947.. [Find this article online](#)

Yu, Z., P. S. Schopf, and J. P. McCreary Jr., 1997: On the annual cycle in the eastern Pacific Ocean. *J. Phys. Oceanogr.*, **27**, 309–324.. [Find this article online](#)

Zeng, X., M. Zhao, and R. E. Dickinson, 1998: Intercomparison of Bulk aerodynamic algorithms for the computation of sea surface fluxes using the TOGA COARE and TAO data. *J. Climate*, **11**, 2628–2644.. [Find this article online](#)

Tables

Table 1. Mean values of terms in the vertically integrated momentum balance. The integral is over 0–250 m for 165°E–170°W and over 0–200 m for 170°–140°W and 140–110°W. Ninety percent confidence interval is indicated for each estimate. Units are $\times 10^{-2} \text{ N m}^{-2}$.

	(C)	(D)	$\rho(\overline{wC})$	$(\overline{wC})^2$
165°E–170°W	-2.96 ± 0.36	-2.11 ± 1.13	0.43 ± 0.13	0.06 ± 0.01
170°W–140°W	-5.08 ± 0.63	-5.54 ± 0.50	0.53 ± 0.14	0.04 ± 0.01
140°W–110°W	-5.11 ± 0.51	-4.18 ± 0.69	-0.37 ± 0.15	0.06 ± 0.01

[Click on thumbnail for full-sized image.](#)

Table 2. Standard deviation of terms in vertically integrated zonal momentum balance for seasonal and interannual variability in three longitudinal intervals along the equator. The integral is over 0–250 m for 165°E–170°W and 0–200 m for 170°–140°W and 140–110°W. Units are $\times 10^{-2} \text{ N m}^{-2}$.

	$\langle \tau_x \rangle$	$\langle \bar{p}_x \rangle$	$\rho \langle \bar{u}_x \rangle$	$\rho \langle \bar{u} \bar{u}_x \rangle$	$\langle \tau_x^2 \rangle$
(a) Seasonal					
165°E–170°W	0.34	0.95	0.46	0.11	<0.01
170°W–140°W	0.62	0.55	0.49	0.09	0.01
140°W–110°W	1.01	0.82	0.35	0.14	0.01
(b) Interannual					
165°E–170°W	1.75	2.02	0.07	0.20	<0.01
170°W–140°W	1.02	1.18	0.08	0.12	<0.01
140°W–110°W	0.68	0.64	0.09	0.17	<0.01

[Click on thumbnail for full-sized image.](#)

Table 3. Cross correlation between zonal wind stress and depth-integrated pressure gradient in three zonal intervals along the equator on interannual timescales. The vertical integral is over 0–250 m for 165°E–170°W and 0–200 m for 170°–140°W and 140°–110°W. The calculation is over the indicated times of data availability. The 90% significance levels for the correlations are estimated, using the method described in Davis (1976).

Interval	165°E–170°W	170°–140°W	140°–110°W
Data availability	12/88–10/96	12/88–10/96	11/83–10/96
Cross-correlation	0.93	0.88	0.80
95% significance	0.80	0.78	0.66

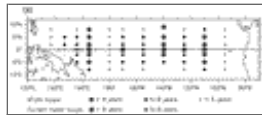
[Click on thumbnail for full-sized image.](#)

Table 4. Cross-correlation coefficients at zero lag between vertically integrated zonal pressure gradient and zonal transport at the equator on interannual timescales. Pressure gradients and transports are vertically integrated over depths of 80 m and 200 m. Subscripts W, E, and 90 mean the west endpoint, the east endpoint, and 90% significance, respectively. Values above the 90% significance are highlighted.

	r_W	r_E	r_{90}
110°W–140°W	-0.21	0.72	0.64
140°W–170°W	0.77	0.85	0.81
170°W–165°E	0.83	0.96	0.96

[Click on thumbnail for full-sized image.](#)

Figures



[Click on thumbnail for full-sized image.](#)

Fig. 1a. The TAO array as of May 1997. Circles are ATLAS thermistor chain buoys, while squares indicate current meter moorings. The size of the symbols indicates length of time a site has been occupied at each location.



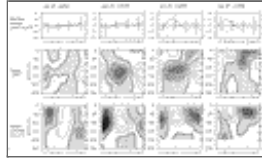
[Click on thumbnail for full-sized image.](#)

Fig. 1b. Time history of sampling at locations used in this study. At $y = 0^\circ$, each buoy has four lines: surface winds (lower thin), SST (medium thick), dynamic height (upper thin), and currents between 80 and 100 m (thick). At $y = \pm 2^\circ$, each buoy has three lines for surface winds, SST, and dynamic height.



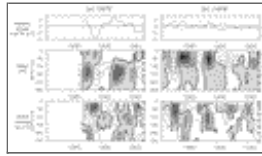
[Click on thumbnail for full-sized image.](#)

Fig. 2. The TAO data at 0°, 110°W. (a) Time series of zonal (solid) and meridional (dashed) surface wind stress ($\times 10^{-2} \text{ N m}^{-2}$), (b) depth–time contours of temperatures (interval: 2°C), and (c) depth–time contours of zonal currents (interval: 0.2 m s^{-1}). Westward currents are lightly shaded and the eastward EUC is heavily shaded. Small squares are depths of measurement.



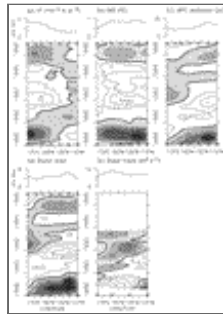
[Click on thumbnail for full-sized image.](#)

Fig. 3. De-meaned seasonal variations from TAO. Upper panels: time series of zonal (solid) and meridional (dashed) wind stress; middle panels: depth–time contours of temperatures (interval: 0.5°C); and lower panels: depth–time contours of zonal currents (interval: 0.1 m s^{-1}). Confidence intervals of 90% are indicated every third month for wind stress. In middle and lower panels, shading indicates negative fluctuations. Small squares indicate depths of measurements.



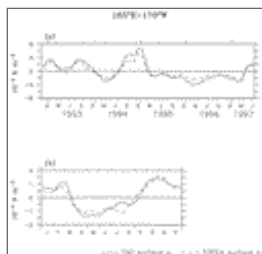
[Click on thumbnail for full-sized image.](#)

Fig. 4. De-meaned interannual variations from TAO. Upper panels: time series of zonal (solid) and meridional (dashed) wind stress; middle panels: depth–time contours of temperatures (interval: 1°C); and lower panels: depth–time contours of zonal currents (interval: 0.1 m s^{-1}). In middle and lower panels, shading indicates negative fluctuations. Small squares indicate depths of measurements.



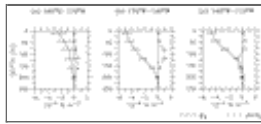
[Click on thumbnail for full-sized image.](#)

Fig. 5. Time series of de-meaned interannual variability of TAO observations along the equator. Negative anomalies are shaded. (a) Zonal stress (interval: $1 \times 10^2 \text{ N m}^{-2}$); (b) SST (interval: 0.5°C); (c) depth of 18°C isotherm (interval: 10 m); (d) surface dynamic height (interval: 3 dyn cm); and (e) zonal transport per unit width over depths of 80–200 m (interval: 5 $\text{m}^2 \text{ s}^{-1}$). In (a)–(d), the squares on the lower (upper) axis are measurement locations at the start (end) of the records, and in (e) the squares on the lower axis indicate the locations for the entire period of time. The curve above each panel is standard deviation of the variation in that panel.



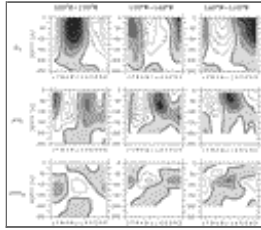
[Click on thumbnail for full-sized image.](#)

Fig. 6. (a) Time series of variations around the long-term mean in sea surface pressure gradient from TAO (solid) and TOPEX/Poseidon (dashed). (b) Mean seasonal cycle from the time series in (a). Units are $\times 10^{-4} \text{ N m}^{-3}$.



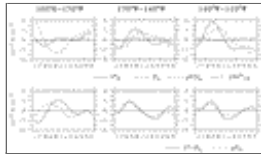
[Click on thumbnail for full-sized image.](#)

Fig. 7. Vertical profiles of mean zonal pressure gradient (solid) and zonal advection (dashed). Units are $\times 10^{-4} \text{ N m}^{-3}$. Horizontal bars indicate 90% confidence intervals.



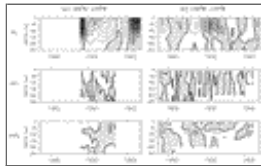
[Click on thumbnail for full-sized image.](#)

Fig. 8. Depth–time contours of seasonal fluctuations in zonally averaged zonal momentum terms. Upper panels: zonal pressure gradient, $\langle p_x \rangle$; middle panels: local acceleration, $\rho \langle u_t \rangle$; lower panels: zonal advection, $\rho \langle uu_x \rangle$. Intervals are $0.2 \times 10^{-4} \text{ N m}^{-3}$.



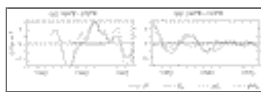
[Click on thumbnail for full-sized image.](#)

Fig. 9. Upper panels: seasonal variations in zonal wind stress $\langle \tau_0^x \rangle$ (solid), depth-integrated pressure gradient $\overline{\langle p_x \rangle}$ (dashed), zonal advection $\rho \overline{\langle uu_x \rangle}$ (dotted), and vertical shear stress, $\langle \tau_{-H}^x \rangle$ (dot–dashed). The H for vertical integral and τ_{-H}^x is set 250 m in $165^\circ\text{E}–170^\circ\text{W}$ and 200 m in $170^\circ–140^\circ\text{W}$ and $140^\circ–110^\circ\text{W}$, respectively. Lower panels: $\tau_0^x - \overline{\langle p_x \rangle}$ (solid) and $\rho \overline{\langle u \rangle}$ (dashed). Units are $\times 10^{-2} \text{ N m}^{-2}$.



[Click on thumbnail for full-sized image.](#)

Fig. 10. Depth–time contours of interannual fluctuations in zonally averaged zonal momentum terms. Upper panels: $\langle p_x \rangle$; middle panels: $\rho \langle u_t \rangle$; lower panels: $\rho \langle uu_x \rangle$. Intervals are $0.5 \times 10^{-4} \text{ N m}^{-3}$.



[Click on thumbnail for full-sized image.](#)

Fig. 11. Interannual fluctuations of zonal momentum terms in (4): zonal wind stress τ_0^x (solid), zonal pressure gradient $\overline{\langle p_x \rangle}$ (dashed), local acceleration $\rho \overline{\langle u_t \rangle}$ (dotted), and zonal advection $\rho \overline{\langle uu_x \rangle}$ (dot–dashed). The depth integral is over the upper 250 m in $165^\circ\text{E}–170^\circ\text{W}$ and 200 m in $140^\circ–110^\circ\text{W}$, respectively. Units are $\times 10^{-2} \text{ N m}^{-2}$.





[Click on thumbnail for full-sized image.](#)

Fig. 12. Time series of vertically integrated zonal pressure gradient (solid) and zonal transport per unit width (dashed: west endpoint; dotted: east endpoint) on interannual timescales. Pressure gradients and transports are vertically integrated over depths of 80 m to 200 m. Units for the pressure gradient and transport are $\times 10^{-3} \text{ N m}^{-2}$ and $\text{m}^2 \text{ s}^{-1}$, respectively.

* PMEL Publication 1969; JISAO Contribution Number 506.

Corresponding author address: Dr. Xuri Yu, UCSB/OPL, 6487 Calle Real, Unit A, Santa Barbara, CA 93117.

E-mail: xuri.yu@opl.ucsb.edu

[top ▲](#)



© 2008 American Meteorological Society [Privacy Policy and Disclaimer](#)

Headquarters: 45 Beacon Street Boston, MA 02108-3693

DC Office: 1120 G Street, NW, Suite 800 Washington DC, 20005-3826

amsinfo@ametsoc.org Phone: 617-227-2425 Fax: 617-742-8718

[Allen Press, Inc.](#) assists in the online publication of AMS journals.